

Design and economic analysis of a hydrokinetic turbine for household applications

Carmen M. Puertas-Frías^{a,b}, Clinton S. Willson^c, Pablo A. García-Salaberri^{a,*}

^a Department of Thermal and Fluids Engineering, Universidad Carlos III de Madrid, 28911 Leganés, Spain

^b Department of data, documentation, and digitalization, Eurofighter GmbH, D-85399 Hallbergmoos, Germany

^c Department of Civil and Environmental Engineering, Louisiana State University, Baton Rouge, LA, 70803, USA

ARTICLE INFO

Keywords:

Renewable energy
Hydrokinetic turbine
Rotor design
Efficiency
Economic analysis
Household energy

ABSTRACT

Social and political concerns on climate change have made renewable energy an essential component of government's work plans. Grid-connected horizontal-axis hydrokinetic turbines are promising eco-friendly power sources for electrical energy supply to households near middle-to-high discharge rivers, while providing an opportunity to sell the energy surplus. In this work, a rotor design analysis of a hydrokinetic turbine with a 1 m nominal radius is performed based on blade element momentum theory. Then, an economic analysis is presented in terms of the discounted payback period and the internal rate of return. The numerical results show that three-bladed hydrokinetic turbines with a nominal tip speed ratio of 5 and state-of-the-art high lift-to-drag ratio hydrofoils (~ 100) lead to maximum performance with a power coefficient around 0.45. Performance can be further improved in an affordable manner using diffuser-augmented hydrokinetic turbines. The use of hydrokinetic energy in household applications can be profitable in leading economic countries with a discounted payback period of 4–6 years. In energy developing countries, this technological solution can be cost effective accompanied by economic subsidies and implementation of a local industry, resulting in similar payback periods.

1. Introduction

In the last decades, hydrokinetic turbines have received increasing attention as clean renewable power sources to meet carbon-free energy demand [1,2]. Hydrokinetic turbines are expected to play a key role in converting the kinetic energy from free flowing and tidal currents in coastal and riverine environments into electrical energy [3]. They are a good option to meet power demand in limited operational spaces, e.g., finite width and depth of a river and/or underwater spaces in conflict with other usages. Horizontal-axis hydrokinetic turbines, which rely on lift forces to extract kinetic energy from a water stream, are more attractive than drag turbines due to their higher efficiency [4]. The higher density of liquid water, $\rho_w \rho_{air}^{-1} \sim 10^3$, allows hydrokinetic turbines to generate a power comparable to wind turbines at lower flow velocities, $V_{us,w} V_{us,air}^{-1} \sim 10$ (assuming a similar power coefficient, C_p). Moreover, hydrokinetic energy offers widespread availability, inexhaustibility and higher predictability than solar and wind energies, thus ensuring a more stable power generation in targeted applications [5].

The first commercial-scale marine current turbine with a 300 kW rated power (11 m rotor diameter) was installed in 2003 near the coast of North Devon (UK) [6]. Since then, deployment of hydrokinetic technology for small (<1 MW) and medium (1–10 MW) energy generation

from marine, tidal and river currents has grown significantly. According to the Electric Power Research Institute (EPRI), 119.9 TWh/year is estimated to be the technically recoverable energy production from rivers of the United States of America (USA) using hydrokinetic technology, with a targeted capacity of 3 GW by 2025 [7,8]. Canada has also recently commissioned a three-phase project to create a nationwide theoretical potential assessment of hydrokinetic energy [9]. In the European Union, two different sized turbines (25 kW and 60 kW) have been developed, which are specifically designed to cater to a niche, low-power, small-scale energy generation market, providing efficient energy generation at reduced flow speeds. The aim of the European Union is to boost the use of hydrokinetic energy in the large amount of small and medium-sized rivers and straits between islands that are available in Europe, thus increasing the current low level of exploitation of this technology (limited to around 5% in Europe) [10]. Besides, the use of hydrokinetic technology is expected to grow in rural areas where there is no access to electricity (e.g., rural populations of African countries), and local regions with good water resources or energy developing countries where hydrokinetic energy can be cost-effective and can help in reducing greenhouse gas emissions (e.g., Brazil

* Corresponding author.

E-mail address: pagsalab@ing.uc3m.es (P.A. García-Salaberri).

<https://doi.org/10.1016/j.renene.2022.08.155>

Received 16 November 2021; Received in revised form 25 June 2022; Accepted 31 August 2022

Available online 6 September 2022

0960-1481/© 2022 The Author(s). Published by Elsevier Ltd. This is an open access article under the CC BY license (<http://creativecommons.org/licenses/by/4.0/>).

(BR) and South Africa) [2]. Nowadays, the main reasons that hinder an extensive use of hydrokinetic energy are: (i) low efficiency, and (ii) low energy capacity. Hence, the application of hydrokinetic turbines for distributed small-scale energy generation is an attractive option for sustainable energy generation (alone or in combination with less predictable renewable sources, such as solar and wind energies). Small-scale hydrokinetic turbines have still to be optimized before extended commercialization and utilization [11]. Unlike wind turbines, hydrokinetic turbines must be properly designed to support the greater loading forces of liquid water, maximize performance at different operating Reynolds numbers, and avoid corrosion and cavitation [12]. This situation has motivated an increasing body of work devoted to the development of high-performance configurations and optimized rotors. A short literature review is presented below.

Mohammadi et al. (2020) [13] analyzed the optimal design of a hydrokinetic turbine located in Golden Gate Strait for operation at low current speed by combining the XFOIL software and blade element momentum theory (BEMT). They showed that optimization of the hydrofoil cross-section (compared to a NACA 4415 hydrofoil) can improve the efficiency by 26% for speeds between 0.5–2 m s⁻¹ and by 50% for speeds between 2–3 m s⁻¹ ($C_p = 0.3$ –0.45). Abutunis et al. (2021) [14] examined experimentally and numerically the design of a coaxial horizontal-axis hydrokinetic turbine system. They found that a three-turbine axial system placed in series can increase the power output by 47% compared to a single-turbine system under optimal-solidity design conditions. Labigalini et al. (2021) [15] used a validated BEMT model and a meta-heuristic algorithm to determine an optimum hydrokinetic turbine adapted to a single person's electricity demand. The best turbine showed a C_p only 18% lower than the Betz Limit ($C_p \approx 0.593$ [16]). Laín et al. (2021) [17] presented a CFD study of the effect of turbine inclination angle with respect to the main flow direction on performance. They found that a 30° inclination angle reduced the C_p from 0.45 to 0.35 and led to alternating stresses that increased fatigue strength. In tandem to optimization, several case studies have examined the applicability of hydrokinetic energy in different scenarios, including rivers, canals, coastal sea currents, irrigation systems, estuaries and outflows from pico and large hydropower plants [18–27]. Most of the works focused their analyses on Latin American countries (BR, Colombia, Ecuador and Mexico), with a lower contribution from Asia (Malaysia and India), Africa (South Africa), North America (California, Louisiana and Alaska) and Europe (Portugal and Austria). These case studies clearly show the potential of hydrokinetic energy for reducing carbon dioxide emissions in the electricity sector, allowing a better use of sustainable resources available in remote locations and providing affordable off-grid generation systems for rural villages and indigenous communities.

In this context, one growing application of hydrokinetic energy is the use of small-scale turbines (radius, $R_{ex} \sim 1$ m) for meeting the energy demand of households, especially in rural areas with good hydraulic resources (see, e.g., [19,28–31]). The scope of this work is to analyze the design and the profitability of hydrokinetic technology for household energy applications in both leading economic countries and energy developing countries, such as USA and BR, respectively. As shown in Fig. 1, the work considers a grid-connected horizontal-axis hydrokinetic turbine for energy harvesting in riverine locations in which the extracted energy is used to meet the energy demand of one or more households, while selling the surplus to the power grid. This type of installation may also be combined with an energy storage system, e.g., a battery and/or an electrolyzer [32–35], although this case is not addressed here. The organization of the paper is as follows. In Section 2, the methodology used for the rotor design based on BEMT is presented. In Section 3, the considerations and variables used in the economic analysis of the hydrokinetic installation are introduced. In Section 4, the results are discussed, including an analysis of the rotor (hydrofoil, tip and hub losses, blade number and tip speed ratio) and an analysis of the investment profitability. Finally, the conclusions and future work are given in Section 5.

2. Rotor design

The flow chart considered for the rotor design of a horizontal-axis hydrokinetic turbine is shown in Fig. 2. The main steps of the methodology are described below, including: (1) rotor sizing and shaping at nominal operating conditions (i.e., the design point), (2) determination of rotor performance using BEMT, and (3) calculation of global output variables, namely power and thrust coefficients, C_p and C_T , respectively. For a given hydrofoil, the input parameters are the power demand, $P\eta^{-1}$, the free-stream velocity, V_{us} , the blade number, z , and the design tip speed ratio, λ_{des} . The fully automated algorithm was coded in Matlab with a computational time lower than 1 min per case (i.e., computation of both $C_p - \lambda$ and $C_T - \lambda$ curves).

1. **Rotor sizing and blade shaping at the design operating condition.** The external radius of the rotor, R_{ex} , is sized according to the targeted power output, P , at the nominal flow velocity of the river, V_{us} . In this step, an approximate value of the rotor power coefficient, C_p , and the overall efficiency of other components (gearbox, generator, power transmission line, etc.), η , must also be taken into account [16]. The radius of the hub, R_{in} , is typically around 20%–25% of the external radius [37,38]. Therefore, the exterior and interior radii of the rotor can be determined as

$$P = \frac{1}{2} \eta C_p \rho \pi R_{ex}^2 V_{us}^3 \Rightarrow R_{ex} = \left(\frac{2P}{\eta C_p \rho \pi V_{us}^3} \right)^{1/2} \quad (1a)$$

$$R_{in} \approx (0.2 - 0.25) R_{ex} \quad (1b)$$

where $\rho \approx 998$ kg m⁻³ is the river water density.

For a given hydrofoil, the design tip speed ratio, $\lambda_{des} = \Omega R_{ex} / V_{us}$, and the blade number, z , are determined according to the application needs. The selection of the hydrofoil must be made to maximize the lift-to-drag ratio, $(C_L/C_D)_{des} = (C_L/C_D)^{max}$, at the characteristic Reynolds number

$$Re = \frac{\rho V_{us} c^{avg}}{\mu} \quad (2)$$

where $\mu \approx 10^{-3}$ kg m⁻¹ s⁻¹ is the river water viscosity and c^{avg} is the average chord length.

The blade shape along the radial coordinate, r , is determined using Schmitz–Glauert's rotor theory [16]. The design parameters include: (1) the angle of the relative flow, $\varphi(r)$; (2) the chord length distribution, $c(r)$; (3) the pitch angle, $\theta_p(r)$; and (4) the twist angle, $\theta_T(r)$. The expressions of these parameters in terms of the local speed ratio at the design point, $\lambda_{des,r} = (r/R_{ex})\lambda_{des}$, are as follows (see, e.g., [16,39,40])

$$\varphi_{des}(r) = \frac{2}{3} \operatorname{atan} \left(\frac{1}{\lambda_{des,r}} \right) \quad (3a)$$

$$c(r) = \frac{8\pi r}{z C_{L,des}} (1 - \cos \varphi_{des}) \quad (3b)$$

$$\theta_p(r) = \varphi_{des} - \alpha_{des} \quad (3c)$$

$$\theta_T(r) = \theta_p - \theta_{p,0} \quad (3d)$$

where $\theta_{p,0}$ is the tip twist angle, and $C_{L,des}$ and α_{des} are the design lift coefficient and angle of attack (corresponding to optimal conditions, $(C_L/C_D)_{des} \sim 10$ –100). Note that the reference tip twist angle is equal to $\theta_{p,0}$ in Eq. (3d) to ensure that the tip twist angle is small due to constructive limitations, $\theta_T(R_{ex}) \approx 0$, but other options are also possible.

The characteristics of the hydrofoil can be extracted from the lift and drag polar plots at the corresponding average Reynolds number from experiments and CFD simulations. Here, the hydrofoil polar plots were taken from the online database *Airfoil Tools* [41] at discrete Reynolds numbers, $Re = 5 \times 10^4$, 10^5 , $2 \times$



Fig. 1. Energy flow from generation in a hydrokinetic turbine, transport through a power transmission line and final use in a household. The hydrokinetic turbine shown in the diagram belongs to the company Smart Hydro Power GmbH [36].

Rotor Design

Input Specifications for a given hydrofoil

Power demand, $P\eta^{-1}$, Free-stream velocity, V_{us} , Blade number, z , & Tip speed ratio, λ_{des}

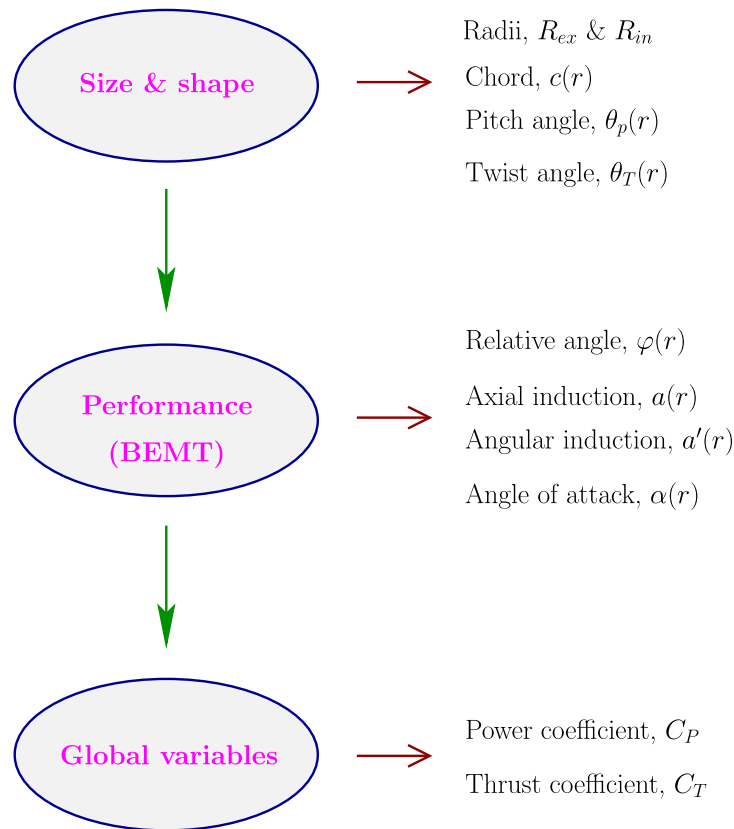


Fig. 2. Flow chart of the rotor design, indicating the variables determined in each step of the process: (1) sizing and shaping at the design point, (2) determination of local performance, and (3) calculation of global output variables.

10^5 , 5×10^5 and 10^6 ($\alpha \approx -5^\circ$ – 10°), and then bilinearly interpolated using the *scatteredInterpolant* function in Matlab. A nearest extrapolation method was implemented for data evaluation outside the available range of Re and α . Since Re depends on c^{avg} (see Eq. (2)), which in turn depends on $C_{L,des}$ according to Eq. (3b), the characteristic Re , together with the corresponding

$C_{L,des}$ and α_{des} values, were determined iteratively. Convergence was reached with no more than 2–3 iterations. The optimal blade shape determined according to Schmitz–Glauert’s theory, Eqs. (3a)–(3d), can be conveniently adjusted to meet fabrication specifications. For example, as shown in Fig. 3(b), the pitch angle can be scaled and restricted to be below

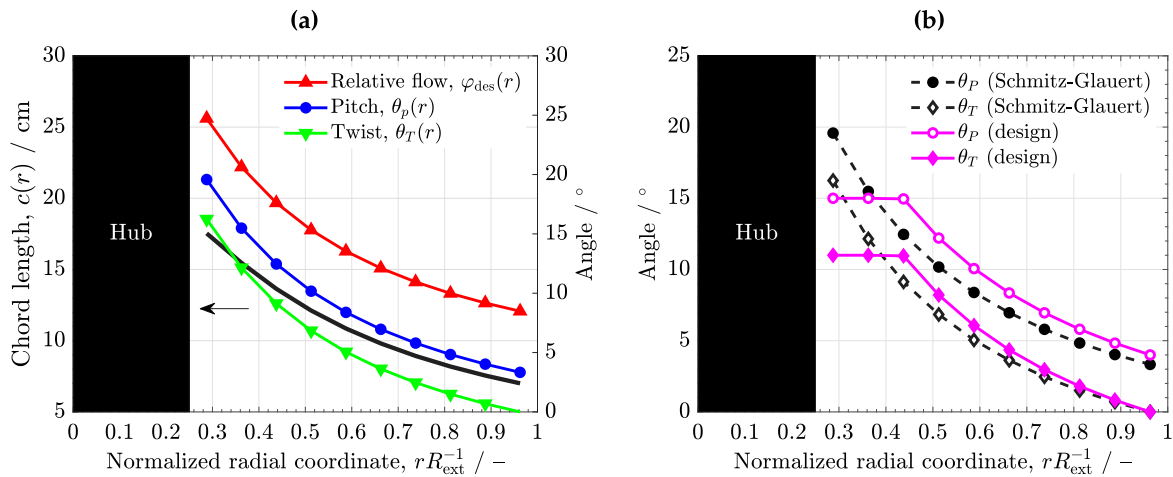


Fig. 3. (a) Radial profiles of the chord length, $c(r)$, the relative flow angle, $\varphi_{des}(r)$, the pitch angle, $\theta_p(r)$, and the twist angle, $\theta_T(r)$, according to Schmitz–Glauert’s theory (see Eqs. (3a)–(3d)). (b) Radial profiles of the actual pitch and twist angles used in a rotor design compared to those determined from Schmitz–Glauert’s theory. The modified profiles correspond to $\beta = 1.2$ and $\theta_p^{max} = 15^\circ$ in Eq. (4). The number of blade elements is equal to $N = 10$ ($\Delta r = 8$ cm).

a cut-off value to avoid exceedingly high twist angles near the hub. The modified θ_p is given by

$$\theta_p = \min(\beta\theta_{p,SG}, \theta_p^{max}) \quad (4)$$

where $\theta_{p,SG}$ is the pitch angle determined from Schmitz–Glauert’s theory, β is a scaling parameter, and θ_p^{max} is the specified maximum pitch angle.

2. **Rotor performance.** Rotor performance can be determined numerically using BEMT [16,42,43]. The derivation of the hydrokinetic turbine was discretized into N elements of equal length along the radial coordinate ($\Delta r = \text{const.}$ with $r \in [R_{in}, R_{ex}]$). The number of blade elements was fixed to $N = 10$ ($\Delta r = 8$ cm), since no noticeable difference was observed using $N = 12$ elements. For a given tip speed ratio, the set of Eqs. (A.13a)–(A.13c) was solved iteratively on each blade element ($n = 1, \dots, N$) to calculate: (1) the local relative flow angle, φ_n ; (2) the local axial induction factor, a_n ; and (3) the angular induction factor, a'_n . The numerical scheme was based on the fixed-point method, combined with the bisection method to solve for a in Eq. (A.13a). For the design point ($\lambda = \lambda_{des}$), the iterative method was initialized by using the solution given by Schmitz–Glauert’s theory with a negligible drag force ($C_D \ll C_L$)

$$\varphi_0 = \frac{2}{3} \text{atan} \left(\frac{1}{\lambda_{des,n}} \right) \quad (5a)$$

$$a_0 = \left(1 + \frac{4 \sin^2 \varphi_0}{\sigma_n C_{L,des} \cos \varphi_0} \right)^{-1} \quad (5b)$$

$$a'_0 = \left(\frac{4 \cos \varphi_0}{\sigma_n C_{L,des}} - 1 \right)^{-1} \quad (5c)$$

where $\sigma_n = zc/(2\pi r)$ is the local rotor solidity.

For subsequent values of λ ($\lambda \neq \lambda_{des}$), the solution calculated for the preceding λ was used as the initial guess in order to improve convergence. To compute a full C_p or $C_T - \lambda$ curve, the range $\lambda \leq \lambda_{des}$ was first analyzed by gradually decreasing λ from λ_{des} . Then, the range $\lambda \geq \lambda_{des}$ was analyzed by gradually increasing λ from λ_{des} .

The sequence to update the variables in the fixed-point scheme is as follows. First, the local relative flow angle is determined from Eq. (A.13c)

$$\varphi_n = \text{atan} \left(\frac{1 - a_n}{(1 + a'_n)\lambda_n} \right) \quad (6)$$

Next, the tip and hub losses factors, F_{tip} and F_{hub} , are calculated using Prandtl’s correction function to account for finite blade number, z , and edge effects (see, e.g., [16,38])

$$F_{tip,n} = \frac{2}{\pi} \text{acos} \left\{ \exp \left[-\frac{(z/2)(1 - r_n/R_{ex})}{(r_n/R_{ex}) \sin \varphi_n} \right] \right\} \quad (7a)$$

$$F_{hub,n} = \frac{2}{\pi} \text{acos} \left\{ \exp \left[\frac{(z/2)(1 - r_n/R_{in})}{(r_n/R_{in}) \sin \varphi_n} \right] \right\} \quad (7b)$$

$$F_n = F_{tip,n} F_{hub,n} \quad (7c)$$

where r_n is the radial coordinate at the center of element n . The local lift and drag coefficients, $C_{L,n}(\alpha_n, Re)$ and $C_{D,n}(\alpha_n, Re)$, are calculated as described in Step 1 by interpolation of the hydrofoil polar plots from [41] at the characteristic Re and the local angle of attack determined from Eq. (3c)

$$\alpha_n = \varphi_n - \theta_{p,n} \quad (8)$$

Subsequently, the local axial induction factor, a , is determined by solving Eq. (A.13a) in each blade element with the bisection method (prescribing a small tolerance error of 10^{-15})

$$\frac{a_n}{1 - a_n} - \frac{\sigma_n}{4F_n \sin^2 \varphi_n} [C_{L,n} \cos \varphi_n + C_{D,n} \sin \varphi_n] - \frac{\psi_n}{(1 - a_n)^2} = 0 \quad (9)$$

where

$$\psi_n = \frac{1}{2F_n} \left(\frac{\max(0, a_n - 0.4)}{0.6} \right)^2 \quad (10)$$

This approach is numerically more stable compared to including the effect of a turbulent wake at high a as part of the main fixed-point iterative scheme [16,42].

Once φ and a are known, the local angular induction factor, a' is updated from the element-wise version of Eq. (A.13b)

$$a'_n = \left(\frac{4F_n \cos \varphi_n \sin \varphi_n}{\sigma_n (C_{L,n} \sin \varphi_n - C_{D,n} \cos \varphi_n)} - 1 \right)^{-1} \quad (11)$$

The stability and convergence of the fixed-point algorithm was improved by introducing an under relaxation factor $\gamma = 0.3$ for the solution variables $\Gamma = \varphi, a$ and a' [44], so that

$$\Gamma_{new} = (1 - \gamma)\Gamma_{old} + \gamma\Gamma_{new}^{com} \quad (12)$$

where Γ_{old} and Γ_{new}^{com} are the value from the previous iteration and the value computed in the current iteration, respectively.

The error of the global numerical scheme was measured using the infinity norm of the absolute variation of the local and angular induction factors between two consecutive iterations

$$E = \max(E_a, E_{a'}) \quad (13a)$$

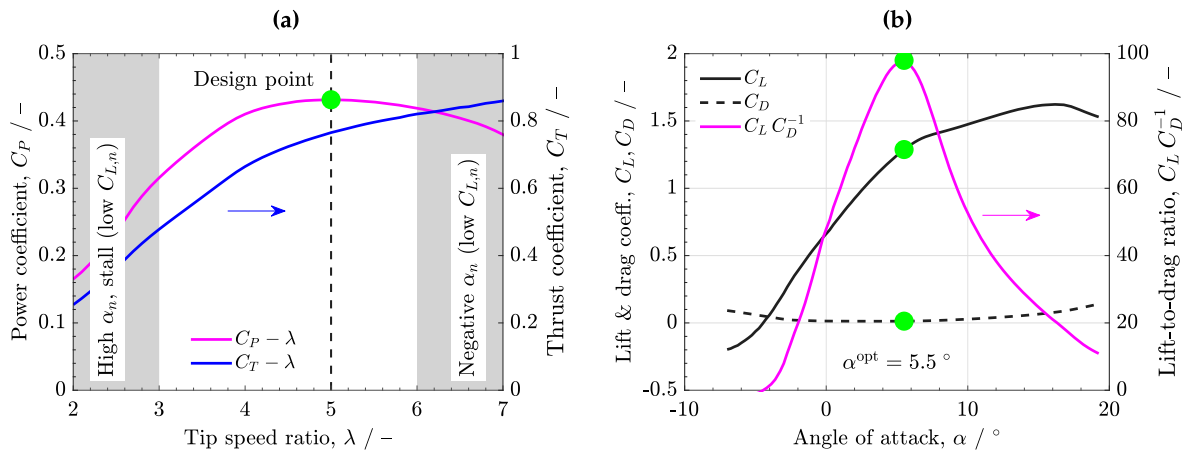


Fig. 4. (a) Variation of the power and thrust coefficients, C_T and C_L , with the tip speed ratio, λ . The regions where the performance decreases significantly due to stall (low λ) and the appearance of negative angles of attacks (high λ) are indicated in gray. (b) Variation of the lift and drag coefficients, C_L and C_D , and the lift-to-drag ratio, C_L/C_D , as a function of the angle of attack, α . The green dots show the design point, corresponding to $\lambda_{des} = 5$ at maximum lift-to-drag ratio, $(C_L/C_D)^{max} = C_L/C_D(\alpha^{opt} \approx 5.5^\circ) \sim 100$. SG-6043 hydrofoil with $\beta = 1.2$ and $\theta_p^{max} = 15^\circ$.

where

$$E_a = \max(|a_{n,new} - a_{n,old}|) \text{ and } E_a' = \max(|a'_{n,new} - a'_{n,old}|);$$

$$n = 1, \dots, N \tag{13b}$$

The stop criterion was set equal to $E \leq 10^{-4}$, resulting in a negligible variation of the total power and thrust coefficients, C_p and C_T , determined as presented in the next section.

- Global output parameters.** The thrust and power coefficients, C_T and C_p , are calculated using Eqs. (A.15a)–(A.15b), where the integrals can be discretized using the mid-point rule over the equal length blade elements

$$C_T = \frac{8\Delta\lambda_r}{\lambda^2} \sum_{n=1}^N F_n \lambda_{r,n} [a_n(1 - a_n) + \psi_n] \tag{14a}$$

$$C_p = \frac{8\Delta\lambda_r}{\lambda^2} \sum_{n=1}^N F_n \lambda_{r,n}^3 a_n'(1 - a_n) \tag{14b}$$

where $\Delta\lambda_r = (\lambda - \lambda_{in})/N$ is the integration increment.

Fig. 4(a) shows representative curves ($C_p - \lambda$ and $C_T - \lambda$) of a hydrokinetic turbine with a SG-6043 hydrofoil computed for $\lambda_{des} = 5$ and $Re \sim 2 \times 10^5$, along with the corresponding $C_L/C_D - \alpha$ curve of the hydrofoil in Fig. 4(b) ($(C_L/C_D)_{des} \sim 100$). C_T increases with λ in the examined range, while C_p reaches a local maximum near the design point [45,46]. The gray patches indicate the λ ranges where the numerical solution is more problematic (see, e.g., [42,47]) due to the appearance of high angle of attacks (i.e., stall) at low tip speed ratios (high α , low λ) and negative angle of attacks (nearly zero and negative C_L) at high tip speed ratios (low α , high λ). C_p strongly decreases when C_L/C_D drops [48,49], so the analysis of these regions is not relevant under the steady-state conditions considered here.

3. Economic analysis

The socio-economic profitability of a hydrokinetic installation was examined for two different scenarios, an economic power, such as USA, and a country with a developing mixed economy, such as BR. The economic data used in the analysis are listed in Table 1. The selected hydrokinetic turbine is commercialized by the company Smart Hydro Power GmbH (Germany) for rivers and canals (SMART Free Stream turbine) [36]. This turbine features 1 m rotor diameter with 3 blades and 5 kW maximum power at the generator output at $V_{us} = 3.1 \text{ m s}^{-1}$ ($P = 0.25\text{--}5 \text{ kW}$, $\Omega = 90\text{--}230 \text{ rpm}$). These characteristics correspond to $C_p \approx 0.45$ and $\eta \approx 0.95$ in Eq. (1a). The range of operating velocities for

this turbine lies within that usually found in middle-to-high discharge rivers in USA and BR, such as the Mississippi and Amazon Rivers. For example, the velocity of the Mississippi River at the Baton Rouge area ranges between $1\text{--}3.6 \text{ m s}^{-1}$ with a mean velocity of 2.25 m s^{-1} [50–52], while the velocity of the Amazon River at the Itacoatiara municipality ranges between $1\text{--}2.5 \text{ m s}^{-1}$ with velocities higher than 2 m s^{-1} during 211 days a year [53,54]. Here, two levels of electricity generation of the hydrokinetic installation were examined, $P = 3 \text{ kW}$ and 5 kW , which correspond to $V_{us} \approx 2.7 \text{ m s}^{-1}$ and 3.25 m s^{-1} , considering a similar $C_p \approx 0.45$ but a lower value of η than before due to power transmission from the turbine to the household(s). η is estimated to be around $\eta = \eta_1 \eta_2 \eta_3 \approx 0.85$, including typical values of the efficiency of the gearbox ($\eta_1 \approx 0.96$), generator ($\eta_2 \approx 0.9$) and power dissipated by Joule heating in the transmission line ($\eta_3 \approx 0.98$) [55].

The initial investment of the hydrokinetic turbine (14,988.00 \$), and the generator and grid connection system (3,912.00 \$), together with 7% industrial profit margin (1,323.00 \$) and import taxes (2,000.00 \$), is estimated to be $I_o = 22,223.00 \text{ \$}$ (considering a 1.2 Euro-to-US dollar exchange rate for the cost of the turbine and the connection system) [36,56–60]. The annual expense in the cash-flow is due to the prorated maintenance service of the system, which was set to $250 \text{ \$ year}^{-1}$ (1–1.5% of the initial investment) [59]. The annual income to the cash-flow is given by the sale of the generated electricity, which is divided into two contributions: (i) the electrical energy provided to the households, and (ii) the energy surplus sold to the power grid (the same average price was assumed for both incomes). It is worth noting that the first income can be interpreted either as the profit of an energy company or the energy saving of a cooperative formed by household owners (e.g., in rural locations). The average electricity prices in USA and BR are rather similar, amounting $0.132 \text{ \$ kWh}^{-1}$ and $0.121 \text{ \$ kWh}^{-1}$ in 2020, respectively [61]. However, the annual household energy consumptions are significantly different between both countries, being around $10,715.00 \text{ kWh year}^{-1}$ in USA and $2,620.00 \text{ kWh year}^{-1}$ in BR, according to The World Bank Group [62]. The four-fold larger average electricity consumption in North American households is directly related with the ten-fold higher per capita income ($63,543.58 \text{ \$ person}^{-1}$ in USA vs. $6,796.84 \text{ \$ person}^{-1}$ in BR) at a similar electricity cost. The above estimations of the electricity price and consumption lead to an annual income per household of $1,414.40 \text{ \$ year}^{-1}$ and $317.00 \text{ \$ year}^{-1}$ in USA and BR, respectively. According to the International Monetary Fund, the discount rate of BR has been around five times larger compared to USA in the last five years due to the higher risk of investment and future cash-flows ($i_{USA} \approx 2\%$ and $i_{BR} \approx 10\%$ were considered) [63].

Table 1

Data used in the economic analysis for the calculation of the initial investment, the maintenance cost, the electricity price per kWh and per household, and the discount rate of the investment in USA and BR.

Concept	Cost (\$)	Reference
SMART free stream turbine generator, structure against debris, anchor cables, 50 m of electric cable	14,988.00	[36]
SMART electrical cabinet grid-connected system inverter, controller, dump load and fuse box	3,912.00	[36]
Total equipment	18,900.00	
7% industrial profit	1,323.00	[56,57]
Taxes	2,000.00	[58]
TOTAL initial investment, I_o	22,223.00	
Annual maintenance	250.00	[59]
Average electricity price per kWh (USA/BR)	0.132/0.121	[61,62]
Annual electricity price per household (USA/BR)	1,414.40/317.00	[61,62]
Discount rate (USA/BR)	2%/10%	[63]

Table 2

Fluid properties and design parameters used for the baseline case and the parametric study of the rotor analysis. The variables examined in the parametric analysis are underlined.

Parameter	Symbol	Value
Water density/kg m ⁻³	ρ	998.2
Water viscosity/kg m ⁻¹ s ⁻¹	μ	1.0034 × 10 ⁻³
Hydrofoil		SG-6043, EPPLER-E836
Tip radius/m	R_{ex}	1
Hub radius/m	R_{in}	0.25
Design tip speed ratio/-	λ_{des}	5 ^a
Number of blades/-	z	3 ^a
River velocity/m s ⁻¹	V_{us}	2.25 (Mississippi River) [‡]

^aThe design tip speed ratio and the number of blades were varied between $\lambda_{des} = 1-12$ and $z = 1-5$, respectively.

The profitability of the investment was evaluated with two figure of merits: (i) the discounted payback period, T_{pb} , and (ii) the internal rate of return, IRR [64]. These two parameters are key indicators to assess the impact of the discount rate and the cash-flow in the amortization time, especially in energy developing countries.

T_{pb} is calculated by determining the year, y , for which the current net present value (NPV) becomes equal to zero after the initial investment in the year $y = 0$, I_o , according to the expression

$$NPV(y) = -I_o + \frac{C[1 - (1+i)^{-y}]}{i} \tag{15}$$

where i is the discount rate and C is the constant annual cash-flow during the operation of the hydrokinetic turbine (equal to the income of the energy sold (or saved) minus the maintenance expense).

IRR is calculated by determining the discount rate for which the NPV vanishes for a prescribed number of amortization years $y = N_{pb}$

$$NPV(N_{pb}) = 0 \Rightarrow IRR = i \tag{16}$$

The function `fzero` was used in Matlab to determine IRR for given values of C and I_o due to the absence of analytical solution. The computational time was virtually negligible with stable convergence.

4. Discussion of results

The baseline data used in the rotor design analysis are listed in Table 2. The study considers a horizontal-axis hydrokinetic turbine with exterior and interior blade radii of 1 m and 0.2 m, respectively, which is located in a river with a nominal velocity $V_{us} \approx 2.25 \text{ m s}^{-1}$ [50]. The baseline number of blades and the design tip speed ratio are equal to $z = 3$ and $\lambda_{des} = 5$. These two variables are further explored in a parametric analysis considering the extended range $z = 1-5$ and $\lambda_{des} = 1-12$. In addition, two high C_L/C_D hydrofoils commonly used in hydrokinetic turbines are examined, SG-6043 and EPPLER-E836, with $(C_L/C_D)^{max} \approx 40-170$ and $(C_L/C_D)^{max} \approx 30-60$ at $Re = 5 \times 10^4 - 10^6$, respectively (see, e.g., [14,41,65–67]).

Fig. 5(a) shows the $C_p - \lambda$ curves of the two selected hydrofoils (SG-6043 and EPPLER-E836) at $Re \sim 2 \times 10^5$, along with an analysis of

the tip and hub losses and the drag coefficient of the turbine with the SG-6043 hydrofoil in Fig. 5(b). The Betz (λ -independent) and Schmitz–Glauert (λ -dependent) limits are also included for comparison. The maximum C_p in both theories is given by [16]

$$C_p^{max} = \begin{cases} \frac{16}{27} & \text{Betz's theory} \\ \frac{24}{\lambda^2} \int_{a_1}^{a_2} \left[\frac{(1-a)(1-2a)(1-4a)}{(1-3a)} \right]^2 da & \text{Schmitz - Glauert's theory} \end{cases} \tag{17a}$$

where $a_1 = 0.25$ is the axial induction factor that makes $\lambda_r = 0$, and a_2 depends on λ through the following expression

$$\lambda^2 - \frac{(1-a_2)(1-4a_2)}{(1-3a_2)} = 0 \tag{17b}$$

As shown in Fig. 5, the performance of the SG-6043 hydrofoil is somewhat higher due to its superior hydrodynamic performance, i.e., higher C_L/C_D at the design point. Quantitatively, the power coefficient increases by 7% ($C_{p,SG} \approx 0.43$ vs. $C_{p,E} \approx 0.4$). The moderate increase of C_p shows that state-of-the-art high C_L/C_D hydrofoils (many of them taken from wind turbines) are already optimized and the global benefit that can be obtained by improving the hydrofoil cross-section is limited (see, e.g., [13,68]). The computed $C_p - \lambda$ curves are in agreement with the experimental data recently presented by Kolekar et al. [66] and Modali et al. [67] (see model validation in Appendix B). In addition, composite materials traditionally used for wind turbines are also a good option for hydrokinetic turbines owing to their high strength-to-weight ratio, corrosion resistance, excellent fatigue resistance and design flexibility. In this regard, research is needed to test the durability of hydrokinetic turbines in long-term pilot projects and evaluate the detrimental impact of corrosion and cavitation that may arise in practice (especially in sea water applications) [69,70]. As shown in Fig. 5(b), the losses due to vanishing circulation at the blade tip and hub have a much higher detrimental effect on C_p , a physical fact that cannot be avoided in practice [71,72]. When there are no losses and C_D is exceedingly small, C_p approaches the Schmitz–Glauert limit.

An affordable approach to improve the technology can be the use of diffuser-augmented hydrokinetic turbines [73,74]. In this technology variant, the rotor is placed inside a diffuser, which helps to reduce the tip vortex and increase the mass-flow capacity. This optimization approach is especially useful for small horizontal-axis hydrokinetic turbines ($R_{ex} \sim 1$ m) placed in low and middle speed rivers, a strategy that cannot be used in large wind turbines ($R_{ex} \sim 20-45$ m) [16]. Previous experimental and numerical works with diffuser-augmented hydrokinetic turbines have shown that the power coefficient can be systematically increased around the Betz limit or even beyond it with an appropriate diffuser design (increase of C_p by a factor of 1.5–2 compared to a conventional design) [73,75,76]. Moreover, the incorporation of a diffuser can provide additional benefits in the underwater environment, such as protecting the rotor from debris and marine fauna, and protecting the rotor from corrosion.

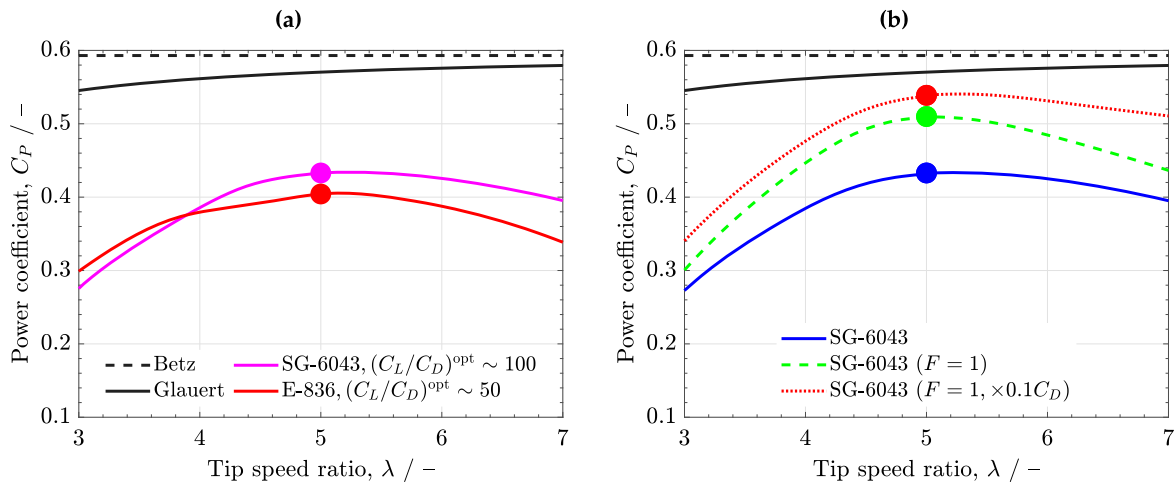


Fig. 5. (a) Power coefficient as a function of the tip speed ratio, $C_p - \lambda$, at $\lambda_{des} = 5$ and $Re \sim 2 \times 10^5$, corresponding to two different hydrofoils, SG-6043 ($(C_L/C_D)^{max} \sim 100$) and EPPLER-E836 ($(C_L/C_D)^{max} \sim 50$). (b) Comparison of the $C_p - \lambda$ curve of the SG-6043 hydrofoil including tip and hub losses (black curve), neglecting the losses factor (green curve), and neglecting the losses factor and introducing a ten-fold decrease of the drag coefficient (red curve). The Betz and Schmitz–Glauert limits are shown by dashed and solid black lines, respectively. $\beta = 1.2$ and $\theta_p^{max} = 15^\circ$.

Fig. 6(a) shows the variation of the optimal power coefficient, C_p^{opt} , while Fig. 6(b) shows the variation of C_L/C_D and φ , as a function of λ_{des} for $z = 1 - 5$. For all blade numbers, C_p^{opt} reaches a maximum at intermediate tip speed ratios [77]. This behavior is explained by the reduction of wake-rotation losses with increasing λ_{des} , especially in the region close to the hub. Note that wake-rotation losses would vanish for an infinitely fast rotating rotor that generates a finite power with an infinitely small torque (i.e., $a' \rightarrow 0$, see Eq. (A.9b)) [16]. However, when λ_{des} is exceedingly high, φ is reduced due to an increase of the tangential velocity component (see Fig. A.1). As a result, the drag-driven torque, Q_D , increases (higher $\cos \varphi$), while the lift-driven torque, Q_L , decreases (lower $\sin \varphi$); see Eq. (A.6b). Eventually, $\varphi \rightarrow 0$ when $\lambda_{des} \rightarrow \infty$, so that the operation of the rotor is no longer possible due to a high drag resistance [16,78]. The negative effect of drag losses is aggravated by the decrease of C_L/C_D with Re caused by the lower chord length used in rotors at high λ_{des} (i.e., reduction of φ_{des}) [40,41,79].

For turbines with 3 blades or more, the results are rather similar. The optimal design tip speed ratio is around $\lambda_{des}^{opt} \approx 4 - 6$, leading to $C_p^{opt} \approx 0.4 - 0.45$. This range agrees with previous experimental and numerical studies of similar hydrokinetic turbines [17,38,40]. However, for single-bladed and two-bladed turbines, the maximum value achieved for C_p^{opt} is lower, especially in the case of single-bladed turbines, where $C_p^{opt} \approx 0.35$ [80]. This is explained by the detrimental effect of tip and hub losses on rotor performance when the blade number is low. In addition, the optimal range of λ_{des} for one-bladed rotors shifts toward higher values ($\lambda_{des} \approx 7 - 9$) because of the higher C_L/C_D reached for that design (thicker chord, higher Re). Three-bladed turbines with state-of-the-art high C_L/C_D hydrofoils ($(C_L/C_D)^{max} \sim 100$), operating at $\lambda_{des} \approx 4 - 5$ ($C_p \approx 0.43$), are the suggested selection for power harvesting in middle-to-high discharge rivers ($P \sim 5$ kW). The use of a reduced number of blades, while keeping good performance, is preferred due to simplicity, ease of manufacturing and materials saving.

The results of the economic analysis are presented in Figs. 7 and 8. The variation of the current NPV as a function of the operating year of the hydrokinetic installation in USA and BR for $P = 5$ kW is shown in Fig. 7(a) (the inset shows the predictions for $P = 3$ kW). Fig. 7(b) shows the number of electrically supplied households, N_h , indicating the associated percentage of the total energy, R_h , determined as

$$N_h = \text{floor} \left(\frac{P_h}{P} \right); \quad R_h = \frac{N_h P_h}{P} \quad (18)$$

where P_h is the annual energy consumption of a household (see Section 3), and $\text{floor}(x)$ denotes the greatest integer less than or equal to

x . The percentage of the energy surplus transferred to the power grid is given by the difference with respect to the total generated energy (i.e., $R_g = 1 - R_h$).

As shown in Fig. 7(a), there is no significant difference in the discounted payback period, T_{pb} , between USA and BR when $P = 5$ kW, being $T_{pb} \approx 4 - 5$ years and $T \approx 6 - 7$ years, respectively. However, the difference significantly increases when the generated power is reduced to $P = 3$ kW. For USA, T_{pb} moderately increases to 7–8 years. However, for BR, T_{pb} dramatically increases to 15–16 years. This is caused by the amplified effect of the higher discount rate of BR ($i_{BR} = 10\%$ vs. $i_{USA} = 2\%$) when the break-even point of the investment is not achieved in a moderate period of time. This result highlights the importance of increasing incomes during the first years of operation in energy developing countries, e.g., by introducing economic subsidies to emerging renewable technologies. For instance, as shown in Fig. 7(b), the number of electrically supplied households in BR is notably larger, reaching $N_h = 10$ and 16 for $P = 3$ and 5 kW, respectively, compared to $N_h = 2$ and 4 in USA. This represents a percentage of the total energy generation higher than 80% in all the cases. Therefore, in energy developing countries, hydrokinetic installations can be more attractive in the form of cooperatives, accompanied by economic subsidies, leading to social benefit and economic boost. The Amazon basin area in South America (shared by BR, Bolivia, Colombia, Ecuador, Peru and Venezuela) or rural areas in Asia and Oceania illustrate this option. However, in leading economic countries with well established energy economies, this type of investment is better adapted to the portfolio of energy companies for meeting policies on renewable energy in locations near mid to large rivers.

The above situation is further examined in Fig. 8 in terms of the IRR. Fig. 8(a) and (b) show the variation of the IRR as a function of T_{pb} for various constant cash-flows, $C = 2 - 6$ k\$ year⁻¹, corresponding to two different initial investments, $I_o = 20$ k\$ (similar to the present study) and $I_o = 10$ k\$, respectively. The horizontal lines show the discount rates of USA and BR. As discussed before, when $I_o = 20$ k\$, the amortization periods in USA and BR approach each other as the cash-flow is increased, becoming almost equal when $C = 6$ k\$ ($T_{pb} \approx 4$ years). This result confirms the crucial role of increasing the cash-flow in energy developing countries during the first years through the incorporation of economic subsidies and the design of cost-effective high-performance hydrokinetic turbines (e.g., incorporating a diffuser). In fact, as shown on the right panel, the combination of a reduction of the initial investment ($I_o = 10$ k\$) by the development of a local industry of diffuser-augmented hydrokinetic turbines and economic subsidies can decrease the discounted payback period in energy developing countries down to $T_{pb} = 2 - 3$ years.

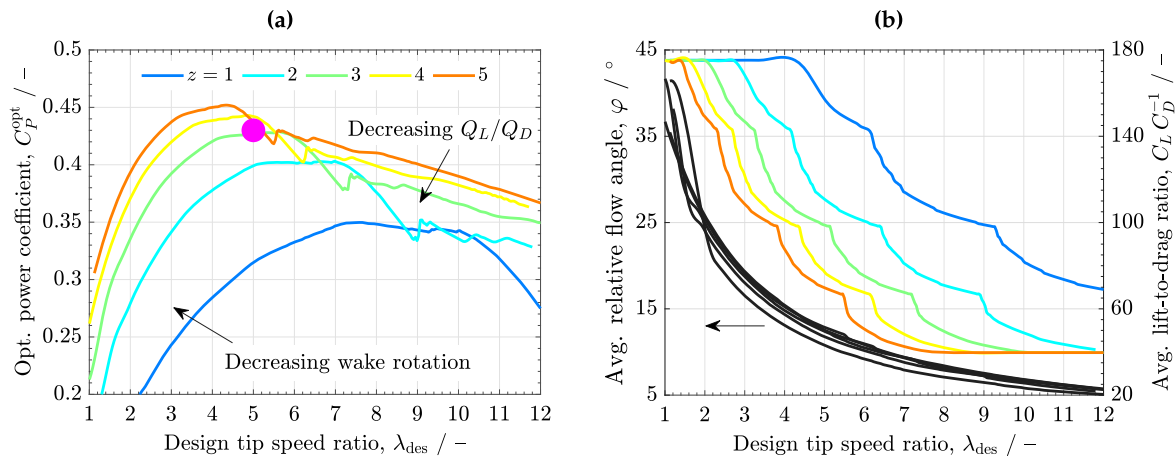


Fig. 6. Variation of (a) the optimal power coefficient, C_p^{opt} , and (b) the average relative flow angle, φ , and lift-to-drag ratio, C_L/C_D , as a function of the design tip speed ratio, λ_{des} , corresponding to various blade numbers, $z = 1 - 5$. The regions where there is an increase of C_p^{opt} due to a reduction of wake-rotation losses and a decrease of C_p^{opt} due to an increase of drag losses (i.e., lower torque ratio, Q_L/Q_D) are indicated. The optimal design point, $\lambda_{des}^{opt} \approx 5$ and $C_p^{opt} \approx 0.43$, is indicated by a magenta dot. SG-6043 hydrofoil with $\beta = 1$ and $\theta_p^{max} \rightarrow \infty$ (i.e., unmodified radial profile).

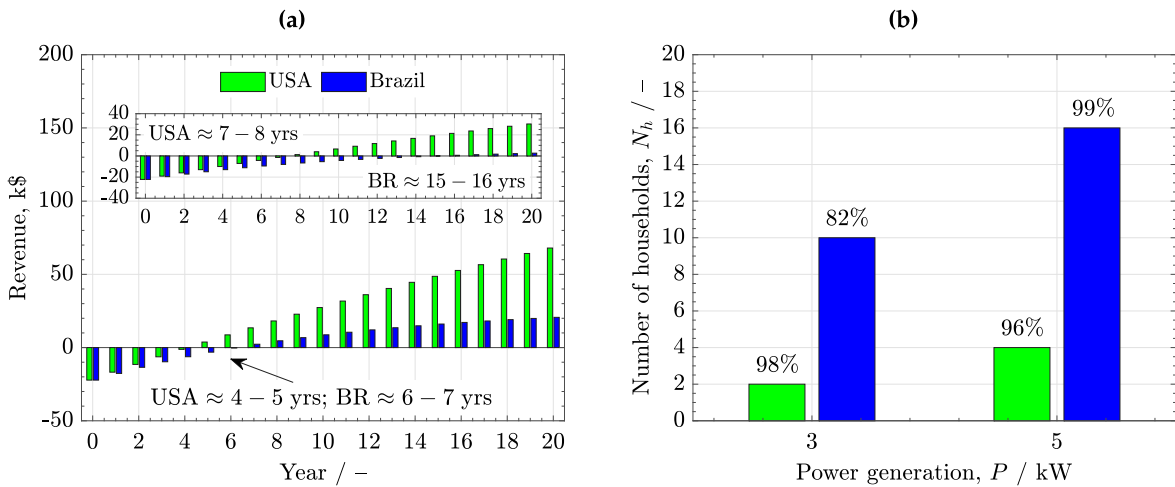


Fig. 7. Comparison between the hydrokinetic installation in USA and BR. (a) Discounted revenue as a function of the operation year, corresponding to a nominal generated power, $P = 5$ kW, and (b) number of supplied households as a function of the generated power, $P = 3$ kW and 5 kW. The inset in (a) shows the discounted revenue for $P = 3$ kW, while the percentage in (b) shows the ratio of the total income coming from households.

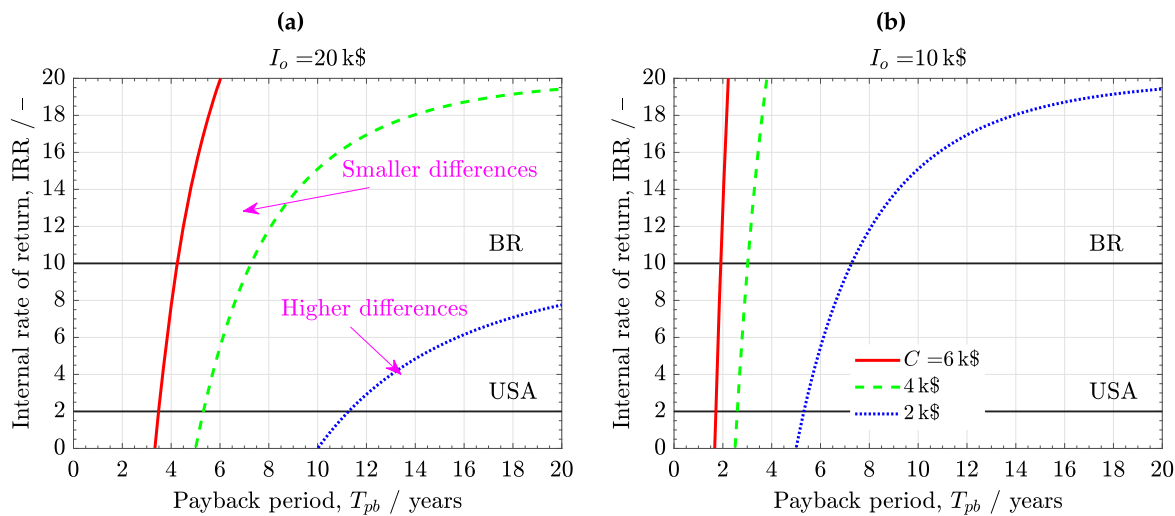


Fig. 8. Variation of the internal rate of return, IRR, as a function of the discounted payback period, T_{pb} , for three different cash-flows, $C = 2, 4, 6$ k\$, corresponding to an initial investment, I_o , of: (a) 20 k\$ and (b) 10 k\$. The discount rates of USA and BR are indicated by black horizontal lines for comparison purposes.

5. Conclusions

Rotor design guidelines and an economic analysis of horizontal-axis hydrokinetic turbines for household applications have been presented. The hydrokinetic turbine had a maximum power output of 5 kW and was located in a middle-to-high discharge river with a nominal velocity around 1–4 m s⁻¹, such as the Mississippi and Amazon Rivers in North and South America, respectively. The rotor performance simulation was carried out using a blade element momentum model, accounting for tip and hub losses and the hydrodynamic characteristics of various state-of-the-art hydrofoils. The sizing and shaping of the blades was performed based on Schmitz–Glauert’s theory for optimal performance.

The results have shown that three-bladed turbines with a rotor radius in the order of 1 m and a design tip speed ratio around 5 are good candidates for energy harvesting in household applications near mid to large rivers. Turbines with these design parameters and high lift-to-drag ratio hydrofoils (~ 100) lead to high power coefficients close to 0.45. This type of hydrokinetic installation can be a profitable option for energy companies in leading economic countries (e.g., USA) as part of their renewable energy portfolio, leading to discounted payback periods of 3–6 years. In energy developing countries (e.g., Brazil, BR), the investment can be particularly attractive (i.e., comparable to USA, with a discounted payback period of 4–7 years) accompanied by economic subsidies that increase the income during the first years of operation. The discounted payback period in energy developing countries can be decreased down to 3–4 years through the development of local industries specialized in hydrokinetic technology, which can provide affordable and cost-effective solutions, such as diffuser-augmented hydrokinetic turbines.

Several research areas warrant closer attention. Future work should consider a more detailed CFD simulation of small- and medium-sized hydrokinetic turbines designed for rivers, along with the study of specific locations and fluctuations during annual power generation. Moreover, the performance of novel diffuser-augmented hydrokinetic turbines should be analyzed numerically and experimentally. The feasibility of combining hydrokinetic energy with energy storage systems (batteries and electrolyzers) should also be examined from a technical and economic point of view.

CRediT authorship contribution statement

Carmen M. Puertas-Frías: Conceptualization, Methodology, Software, Validation, Formal analysis, Investigation, Data curation, Writing – original draft, Writing – review & editing. **Clinton S. Willson:** Conceptualization, Investigation, Writing – original draft, Writing – review & editing, Visualization, Supervision. **Pablo A. García-Salaberri:** Conceptualization, Methodology, Software, Validation, Formal analysis, Investigation, Resources, Data curation, Writing – original draft, Writing – review & editing, Visualization, Supervision, Project administration, Funding acquisition.

Declaration of competing interest

The authors declare that they have no known competing financial interests or personal relationships that could have appeared to influence the work reported in this paper.

Funding

This work was supported by projects PID2019-106740RB-I00 and EIN2020-112247 of the Spanish Agencia Estatal de Investigación. Funding for APC: Universidad Carlos III de Madrid (Read & Publish Agreement CRUE-CSIC 2022).

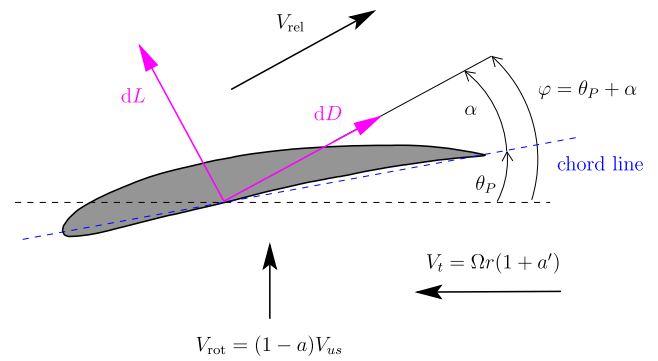


Fig. A.1. Schematic of differential lift and drag forces, dL and dD , that act on a blade element, showing the orientation of the axial velocity, $V_{rot} = (1 - a)V_{us}$, the tangential velocity, $V_t = \Omega r(1 + a')$, and the relative velocity, $\vec{V}_{rel} = \vec{V}_{rot} - \vec{V}_t$, at the rotor plane. The pitch angle, θ_P , the angle of attack, α , and the relative flow angle, $\varphi = \theta_P + \alpha$, are also indicated.

Appendix A. BEMT formulation

According to the momentum theory (MT), for a rotor with an infinite number of blades, the differential thrust, dT , and torque, dQ , are given by

$$dT = \Delta p 2\pi r dr \quad (A.1a)$$

$$dQ = \rho \omega V_{rot} 2\pi r^3 dr \quad (A.1b)$$

where Δp is the pressure drop across the rotor, ω is the fluid (i.e., wake) angular velocity and V_{rot} is the relative velocity between the fluid and the rotating blade.

Applying the Bernoulli equation and the momentum conservation equation on a turbine, two expressions can be obtained for Δp

$$\Delta p = \frac{1}{2} \rho (V_{us}^2 - V_{ds}^2) \quad (\text{energy}) \quad (A.2a)$$

$$\Delta p = \rho V_{rot} (V_{us} - V_{ds}) \quad (\text{momentum}) \quad (A.2b)$$

where V_{us} and V_{ds} are the upstream and downstream fluid velocities, respectively.

Combining Eqs. (A.1a)–(A.1b) and (A.2a)–(A.2b), we yield

$$dT = 4a(1 - a)V_{us}^2 \rho \pi r dr \quad (A.3a)$$

$$dQ = 4a'(1 - a)\lambda_r V_{us}^2 \rho \pi r^2 dr \quad (A.3b)$$

where λ_r is the local speed ratio, and $a = (V_{us} - V_{rot})/V_{us}$ and $a' = \omega/2\Omega$ are the axial and angular induction factors, respectively, with Ω the rotor angular velocity.

According to the blade element theory (BET), dT and dQ can be expressed in terms of the differential lift, dL , and drag, dD , forces that act on a blade element of radial length dr (see Fig. A.1)

$$dT = z [dL \cos \varphi + dD \sin \varphi] \quad (A.4a)$$

$$dQ = zr [dL \sin \varphi - dD \cos \varphi] \quad (A.4b)$$

where z is the number of blade elements, and dL and dD are equal to

$$dL = C_L \frac{1}{2} \rho V_{r,rel}^2 c(r) dr \quad (A.5a)$$

$$dD = C_D \frac{1}{2} \rho V_{r,rel}^2 c(r) dr \quad (A.5b)$$

In this expression, $c(r)$ is the local chord length of the blade element, $V_{r,rel} = V_{rot}/\sin \varphi$ is the relative velocity between the fluid and the rotating blade, and C_L and C_D are the lift and drag coefficients, respectively, which depend on the angle of attack, α , and the Reynolds number, Re .

Therefore, using Eqs. (A.4a)–(A.5b) together with Eqs. (A.2a)–(A.2b), dT and dQ take the following form

$$dT = \sigma \frac{(1-a)^2}{\sin^2 \varphi} [C_L \cos \varphi + C_D \sin \varphi] V_{us}^2 \rho \pi r dr \quad (A.6a)$$

$$dQ = \sigma \frac{(1-a)^2}{\sin^2 \varphi} [C_L \sin \varphi - C_D \cos \varphi] V_{us}^2 \rho \pi r^2 dr \quad (A.6b)$$

where the local rotor solidity is equal to

$$\sigma = \frac{zc(r)}{2\pi r} \quad (A.7)$$

From the above results, two relationships are obtained in BEMT. Combining the results from MT, Eqs. (A.3a)–(A.3b), and BET, Eqs. (A.6a)–(A.6b), we yield

$$\frac{a}{1-a} = \frac{\sigma}{4 \sin^2 \varphi} [C_L \cos \varphi + C_D \sin \varphi] \quad (A.8a)$$

$$\frac{a'}{1-a} = \frac{\sigma}{4\lambda_r \sin^2 \varphi} [C_L \sin \varphi - C_D \cos \varphi] \quad (A.8b)$$

Additionally, the angle of the relative velocity, φ , is related with a and a' through the velocity triangle

$$\tan \varphi = \frac{V_{us}(1-a)}{\Omega r(1+a')} = \frac{1-a}{\lambda_r(1+a')} \quad (A.8c)$$

The set of Eqs. (A.8a)–(A.8c) must be supplemented with the operating conditions, the rotor size and shape, and the lift and drag coefficients of the hydrofoil at the operating angle of attack and Reynolds number, $C_L(\alpha, Re)$ and $C_D(\alpha, Re)$, where $\alpha = \varphi - \theta_p$, with θ_p the pitch angle.

The effect of tip and hub losses, $F = F_{tip}F_{hub}$, is included by correcting MT Eqs. (A.1a)–(A.1b) for a finite number of blades, z , leading to the following modified MT equations

$$dT = 4a(1-a)FV_{us}^2 \rho \pi r dr \quad (A.9a)$$

$$dQ = 4a'(1-a)\lambda_r FV_{us}^2 \rho \pi r^2 dr \quad (A.9b)$$

Therefore, the system of equations in BEMT, Eqs. (A.8a)–(A.8c), takes the corrected form

$$\frac{Fa}{1-a} = \frac{\sigma}{4 \sin^2 \varphi} [C_L \cos \varphi + C_D \sin \varphi] \quad (A.10a)$$

$$\frac{Fa'}{1-a} = \frac{\sigma}{4\lambda_r \sin^2 \varphi} [C_L \sin \varphi - C_D \cos \varphi] \Rightarrow a' = \left[\frac{4F \cos \varphi \sin \varphi}{\sigma(C_L \sin \varphi - C_D \cos \varphi)} - 1 \right]^{-1} \quad (A.10b)$$

$$\tan \varphi = \frac{1-a}{\lambda_r(1+a')} \Rightarrow \varphi = \text{atan} \left(\frac{1-a}{\lambda_r(1+a')} \right) \quad (A.10c)$$

where the relationship between φ , a , a' and λ_r provided by Eq. (A.10c) was introduced into Eq. (A.10b) to derive the final expression for a' in terms of φ , C_L and C_D .

It is well known that MT fails to account for the effect of a turbulent wake when $a > 0.4$ [16]. This conditions was introduced in the model by modifying dT in Eq. (A.9a) by the following expression

$$dT = 4\chi FV_{us}^2 \rho \pi r dr \quad (A.11)$$

where χ is given as a function of a according to the correction proposed by Ledoux et al. [42] based on the work of Buhl [81] (see Fig. A.2)

$$\chi = a(1-a) + \psi; \quad \psi = \frac{1}{2F} \left(\frac{\max(0, a-0.4)}{0.6} \right)^2 \quad (A.12)$$

Hence, the system of Eqs. (A.10a)–(A.10c), including the effect of a turbulent wake for $a > 0.4$, adopts the final form

$$\frac{a}{1-a} = \frac{\sigma}{4F \sin^2 \varphi} [C_L \cos \varphi + C_D \sin \varphi] - \frac{\psi}{(1-a)^2} \quad (A.13a)$$

$$\frac{a'}{1-a} = \frac{\sigma}{4F\lambda_r \sin^2 \varphi} [C_L \sin \varphi - C_D \cos \varphi] \Rightarrow a' = \left[\frac{4F \cos \varphi \sin \varphi}{\sigma(C_L \sin \varphi - C_D \cos \varphi)} - 1 \right]^{-1} \quad (A.13b)$$

$$\tan \varphi = \frac{1-a}{\lambda_r(1+a')} \Rightarrow \varphi = \text{atan} \left(\frac{1-a}{\lambda_r(1+a')} \right) \quad (A.13c)$$

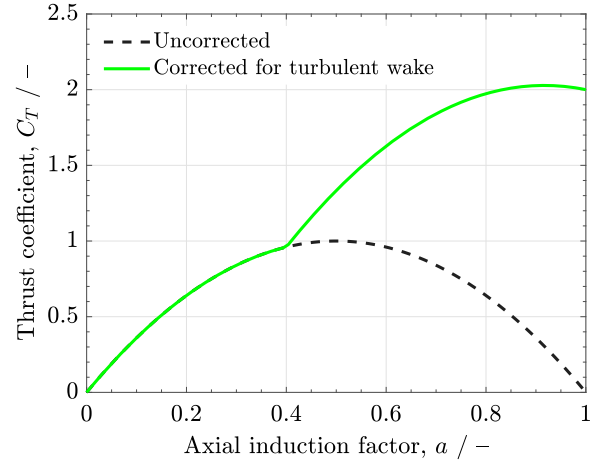


Fig. A.2. Variation of the local thrust coefficient, C_T , with the local axial induction factor, a , including or not including the correction factor for turbulent wake, ψ , when $a > 0.4$ (see Eq. (A.12)). $F = 1$.

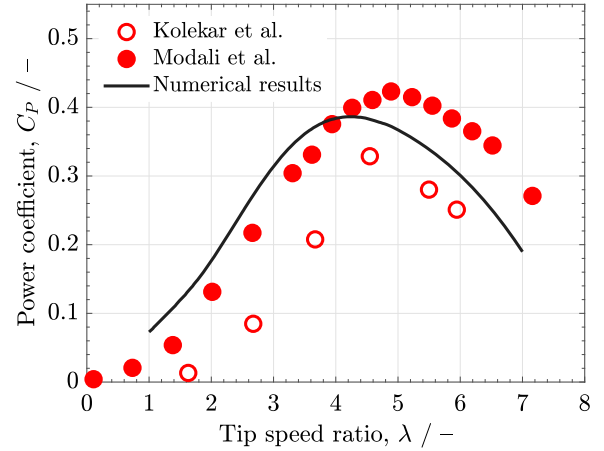


Fig. A.3. Comparison of the power coefficient, C_P , vs. tip speed ratio, λ , predicted by the numerical model with the experimental data of Kolekar et al. [66] and Modali et al. [67].

The global thrust coefficient, C_T , and the power coefficient, C_P , of the turbine are determined by integrating the force and the power of the torque on the rotor, respectively

$$C_T = \frac{1}{\frac{1}{2} \rho V_{us}^2 \pi R_{ex}^2} \int_{R_{in}}^{R_{ex}} dT(r) \quad (A.14a)$$

$$C_P = \frac{1}{\frac{1}{2} \rho V_{us}^3 \pi R_{ex}^2} \int_{R_{in}}^{R_{ex}} \Omega dQ(r) \quad (A.14b)$$

where $dT(r)$ and $dQ(r)$ are the differential thrust and torque distributions along the radial coordinate, Eqs. (A.11) and (A.9b), respectively. Considering the change of variable $\lambda_r = \Omega r / V_{us}$, the following integrals in terms of λ_r are obtained

$$C_T = \frac{8F}{\lambda^2} \int_{\lambda_{in}}^{\lambda} \lambda_r [a(1-a) + \psi] d\lambda_r \quad (A.15a)$$

$$C_P = \frac{8F}{\lambda^2} \int_{\lambda_{in}}^{\lambda} \lambda_r^3 a'(1-a) d\lambda_r \quad (A.15b)$$

where λ_{in} is the inner speed ratio at the hub and λ is the tip speed ratio.

Appendix B. Model validation

Fig. A.3 shows a comparison of the model predictions against the experimental data of Kolekar et al. [66] and Modali et al. [67] for a

hydrokinetic turbine with $2R_{ex} = 0.2794$ m in diameter and an SG-6043 hydrofoil profile. In addition, the turbine featured constant chord ($c = 1.65 \times 10^{-2}$ m), untwisted ($\theta_T = 0^\circ$) blades ($z = 3$) with a pitch angle around $\theta_p \approx 10^\circ$. The free-stream velocity was equal to $V_{us} \approx 0.8$ m s⁻¹. In the simulations, the hub radius was set equal to $R_{in} = 0.2R_{ex}$, including 20 blade elements along the radius.

Good overall agreement is found between the experimental data and the numerical results despite differences at small and large tip speed ratios. The maximum performance is achieved for $\lambda \approx 5$ with $C_p \approx 0.3 - 0.4$.

Nomenclature

a	Axial induction factor/–
a'	Angular induction factor/–
C	Cash-flow/\$
C_D	Drag coefficient/–
C_L	Lift coefficient/–
C_P	Power coefficient/–
C_T	Thrust coefficient/–
c	Chord length/m
D	Drag force/N
E	Error/–
F	Loss factor/–
I_o	Initial investment/\$
IRR	Internal rate of return/–
i	Discount rate/–
L	Lift force/N
N	Number of blade elements/–
N_{pb}	Number of amortization years/–
N_h	Number of supplied households/–
NPV	Net present value/\$
P	Output power/W
P_h	Output power to households/W
p	Pressure/Pa
Q	Torque/N m ⁻¹
R	Radius/m
Re	Reynolds number/–
R_h	Energy ratio supplied to households/–
R_g	Energy ratio supplied to the power grid/–
r	Radial coordinate/m
T	Thrust/N
T_{pb}	Discounted payback period/years
V	Velocity/m s ⁻¹
y	Year number/year
z	Blade number/–
Greek letters	
α	Angle of attack/–
β	Scaling parameter/–
Γ	Variable in Eq. (12)/–
γ	Under relaxation factor
η	Electrical efficiency of the power transmission from the rotor to the household/–
θ_p	Pitch angle/–
θ_T	Twist angle/–
λ	Tip speed ratio/–
λ_r	Local speed ratio/–
μ	Dynamic viscosity/kg m ⁻¹ s ⁻¹
ρ	Density/kg m ⁻³
σ	Solidity/–
φ	Relative flow angle/–
χ	Thrust correction function/–
ψ	Thrust correction function for turbulent wake ($a > 0.4$)/–
Ω	Angular velocity/s ⁻¹
ω	Angular wake velocity/s ⁻¹

Subscripts

D	Drag
des	Design
ds	Downstream condition
ex	Exterior
hub	Rotor hub
in	Interior
L	Lift
n	Index of blade element
new	Current value from new iteration
old	Previous value from old iteration
r	Local condition along the radius
rot	Rotor
tip	Rotor tip
us	Upstream condition
0	Initial guess
Superscripts	
avg	Average
com	Computed
max	Maximum
opt	Optimum
SG	Schmitz–Glauert's theory

References

- [1] G. Saini, R.P. Saini, A review on technology, configurations, and performance of cross-flow hydrokinetic turbines, *Int. J. Energy Res.* 43 (13) (2019) 6639–6679.
- [2] M. Sood, S.K. Singal, Development of hydrokinetic energy technology: A review, *Int. J. Energy Res.* 43 (11) (2019) 5552–5571.
- [3] W. Ibrahim, M. Mohamed, R. Ismail, P. Leung, W. Xing, A. Shah, Hydrokinetic energy harnessing technologies: A review, *Energy Rep.* 7 (2021).
- [4] A. Ramadan, M. Hemida, W. Abdel-Fadeel, W. Aissa, M. Mohamed, Comprehensive experimental and numerical assessment of a drag turbine for river hydrokinetic energy conversion, *Ocean Eng.* 227 (2021) 108587.
- [5] F. Behrouzi, M. Nakisa, A. Maimun, Y.M. Ahmed, Global renewable energy and its potential in Malaysia: A review of hydrokinetic turbine technology, *Renew. Sustain. Energy Rev.* 62 (2016) 1270–1281.
- [6] F. Ponta, P. Jacovkis, Marine-current power generation by diffuser-augmented floating hydro-turbines, *Renew. Energy* 33 (4) (2008) 665–673.
- [7] P. Jacobson, T. Ravens, K. Cunningham, G. Scott, Assessment and mapping of the riverine hydrokinetic resource in the continental United States, 2012, DOI, 10.1219876.
- [8] M. Bahleda, M.A. Hosko, Assessment of Waterpower Potential and Development Needs, Electric Power Research Institute California Final Report, 2007.
- [9] R. Jenkinson, Assessment of Canada's Hydrokinetic Power Potential, National Research Council of Canada. NRC Canadian Hydraulics Centre, 2010.
- [10] A Range of Economically Viable, Innovative and Proven Hydrokinetic Turbines That Will Enable Users to Exploit the Huge Potential of Clean, Predictable Energy in the World's Rivers, Canals and Estuarine, European Commission, 2017.
- [11] A. Muratoglu, M.I. Yuce, Design of a river hydrokinetic turbine using optimization and CFD simulations, *J. Energy Eng.* 143 (4) (2017) 04017009.
- [12] D.A. do Rio Vaz, J.R. Vaz, P.A. Silva, An approach for the optimization of diffuser-augmented hydrokinetic blades free of cavitation, *Energy Sustain. Dev.* 45 (2018) 142–149.
- [13] S. Mohammadi, M. Hassanalian, H. Arionfard, S. Bakhtiyarov, Optimal design of hydrokinetic turbine for low-speed water flow in golden gate strait, *Renew. Energy* 150 (2020) 147–155.
- [14] A. Abutunis, M. Fal, O. Fashanu, K. Chandrashekhara, L. Duan, Coaxial horizontal axis hydrokinetic turbine system: Numerical modeling and performance optimization, *J. Renew. Sustain. Energy* 13 (2) (2021) 024502.
- [15] L.C. Labigalini, R. de Vasconcelos Salvo, R.S. de Lima, R.C. da Silva, I. de Marchi Neto, Hydrokinetic turbine design through performance prediction and hybrid metaheuristic multi-objective optimization, *Energy Convers. Manage.* 238 (2021) 114169.
- [16] J.F. Manwell, J.G. McGowan, A.L. Rogers, *Wind Energy Explained: Theory, Design and Application*, John Wiley & Sons, 2010.
- [17] S. Laín, L.T. Contreras, O.D. López, Hydrodynamic characterisation of a garman-type hydrokinetic turbine, *Fluids* 6 (5) (2021) 186.
- [18] A. Ramadan, M.A. Nawar, M. Mohamed, Performance evaluation of a drag hydrokinetic turbine for rivers current energy extraction—a case study, *Ocean Eng.* 195 (2020) 106699.
- [19] K.W. Tan, B. Kirke, M. Anyi, Small-scale hydrokinetic turbines for remote community electrification, *Energy Sustain. Dev.* 63 (2021) 41–50.
- [20] I. Iglesias, A. Bio, L. Bastos, P. Avilez-Valente, Estuarine hydrodynamic patterns and hydrokinetic energy production: The douro estuary case study, *Energy* 222 (2021) 119972.

- [21] A. Bekker, M. Van Dijk, C.M. Niebuhr, C. Hansen, Framework development for the evaluation of conduit hydropower within water distribution systems: A South African case study, *J. Cleaner Prod.* 283 (2021) 125326.
- [22] A.P.V. Quiceno, V.H.A. Tique, O.F.A. Pérez, R.F.C. Quintero, F.J.V. Hoyos, Development of riverine hydrokinetic energy systems in Colombia and other world regions: a review of case studies, *Dyna* 88 (217) (2021) 256–264.
- [23] G. Saini, A. Kumar, R. Saini, Assessment of hydrokinetic energy—a case study of eastern Yamuna canal, *Mater. Today Proc.* 46 (2021) 5223–5227.
- [24] R.F. Colmenares-Quintero, L.F. Latorre-Noguera, N. Rojas, K. Kollmsee, K.E. Stansfield, J.C. Colmenares-Quintero, Computational framework for the selection of energy solutions in indigenous communities in Colombia: Kanaliotojo case study, *Cogent Eng.* 8 (1) (2021) 1926406.
- [25] J.F. Bárcenas Graniel, J.V. Fontes, H.F.G. Garcia, R. Silva, Assessing hydrokinetic energy in the Mexican Caribbean: A case study in the Cozumel channel, *Energies* 14 (15) (2021) 4411.
- [26] C. Niebuhr, M.V. Dijk, J. Bhagwan, Technical and practical valuation of hydrokinetic turbine integration into existing canal infrastructure in South Africa: A case study, in: *Multidisciplinary Digital Publishing Institute Proceedings*, Vol. 2, 2018, p. 595.
- [27] M. Salleh, N. Kamaruddin, Z. Mohamed-Kassim, Micro-hydrokinetic turbine potential for sustainable power generation in Malaysia, in: *IOP Conference Series: Materials Science and Engineering*, Vol. 370, IOP Publishing, 2018, 012053.
- [28] S.S. Alam, N.H.N. Hashim, M. Rashid, N.A. Omar, N. Ahsan, M.D. Ismail, Small-scale households renewable energy usage intention: Theoretical development and empirical settings, *Renew. Energy* 68 (2014) 255–263.
- [29] E. Martinot, A. Chaurey, D. Lew, J.R. Moreira, N. Wamukonya, Renewable energy markets in developing countries, *Annu. Rev. Energy Environ.* 27 (1) (2002) 309–348.
- [30] K. Kusakana, Feasibility analysis of river off-grid hydrokinetic systems with pumped hydro storage in rural applications, *Energy Convers. Manage.* 96 (2015) 352–362.
- [31] V.B. Miller, E.W. Ramde, R.T. Gradoville Jr., L.A. Schaefer, Hydrokinetic power for energy access in rural Ghana, *Renew. Energy* 36 (2) (2011) 671–675.
- [32] K. Kusakana, Energy management of a grid-connected hydrokinetic system under time-use tariff, *Renew. Energy* 101 (2017) 1325–1333.
- [33] J. Lata-García, F. Jurado, L.M. Fernández-Ramírez, H. Sánchez-Sainz, Optimal hydrokinetic turbine location and techno-economic analysis of a hybrid system based on photovoltaic/hydrokinetic/hydrogen/battery, *Energy* 159 (2018) 611–620.
- [34] G. Tsakyridis, N.I. Xiros, C. Sultan, M. Scharringhausen, J.H. VanZwieten, A hydrogen storage system for efficient ocean energy harvesting by hydrokinetic turbines, in: *The 26th International Ocean and Polar Engineering Conference*, OnePetro, 2016.
- [35] P.A. García-Salaberri, 1D two-phase, non-isothermal modeling of a proton exchange membrane water electrolyzer: An optimization perspective, *J. Power Sources* 521 (2022) 230915.
- [36] Smart hydro power gmbh, 2021, <https://www.smart-hydro.de/es/sistemas-de-energia-renovable/precios-turbinas-fotovoltaico-sistemas-hibrido/>. Accessed: 2021-10-04.
- [37] J.N. Goundar, M.R. Ahmed, Design of a horizontal axis tidal current turbine, *Appl. Energy* 111 (2013) 161–174.
- [38] M. Barbarić, Z. Guzović, Investigation of the possibilities to improve hydrodynamic performances of micro-hydrokinetic turbines, *Energies* 13 (17) (2020) 4560.
- [39] R. Gasch, J. Tvele, Blade geometry according to Betz and Schmitz, in: *Wind Power Plants*, Springer, 2012, pp. 168–207.
- [40] L. Wang, X. Tang, X. Liu, Optimized chord and twist angle distributions of wind turbine blade considering Reynolds number effects, *Wind Energy: Mater. Eng. Policies (WEMEP)* (2012).
- [41] Airfoil tools, 2021, <http://airfoiltools.com/search/airfoils?m=a>. Accessed: 2021-10-04.
- [42] J. Ledoux, S. Riffo, J. Salomon, et al., Analysis of the blade element momentum theory, 2020, arXiv preprint arXiv:2004.11100.
- [43] M. Sriti, et al., Tip loss factor effects on aerodynamic performances of horizontal axis wind turbine, *Energy Procedia* 118 (2017) 136–140.
- [44] E. Branlard, Wind turbine aerodynamics and vorticity-based methods, 2020.
- [45] E.E. Lust, K.A. Flack, L. Luznik, Survey of the near wake of an axial-flow hydrokinetic turbine in quiescent conditions, *Renew. Energy* 129 (2018) 92–101.
- [46] H. Kim, K. Kim, C.L. Bottasso, F. Campagnolo, I. Paek, Wind turbine wake characterization for improvement of the ainslie eddy viscosity wake model, *Energies* 11 (10) (2018) 2823.
- [47] D. Maniaci, An investigation of WT_Perf convergence issues, in: *49th AIAA Aerospace Sciences Meeting Including the New Horizons Forum and Aerospace Exposition*, 2011, p. 150.
- [48] E. Muljadi, A. Wright, V. Gevorgian, J. Donegan, C. Marnagh, J. McEntee, Turbine control of tidal and river power generator, in: *2016 North American Power Symposium (NAPS)*, IEEE, 2016, pp. 1–5.
- [49] D. Kądrowski, M. Kulak, M. Lipian, M. Stępień, P. Baszczyński, K. Zawadzki, M. Karczewski, Challenging low Reynolds-SWT blade aerodynamics, in: *MATEC Web of Conferences*, Vol. 234, EDP Sciences, 2018, p. 01004.
- [50] U.S. Geological survey. Water resources: Mississippi river at Baton Rouge, LA, 2021, <https://waterdata.usgs.gov/monitoring-location/07374000/#parameterCode=00060&period=P365D&compare=true>. Accessed: 2021-10-13.
- [51] P. Karalekas, G.J. Kowalski, E. Lovelace, Modeling hydrokinetic turbine performance in the Mississippi river, *Mar. Technol. Soc. J.* 47 (4) (2013) 57–66.
- [52] V. Neary, B. Gunawan, D. Sale, Turbulent inflow characteristics for hydrokinetic energy conversion in rivers, *Renew. Sustain. Energy Rev.* 26 (2013) 437–445.
- [53] N. Filizola, E. Melo, E. Armijos, J. McGlynn, Preliminary Analysis of Potential for River Hydrokinetic Energy Technologies in the Amazon Basin, Inter-American Development Bank, 2015.
- [54] J. da Silva Cruz, C.J.C. Blanco, A.C.P.B. Junior, Flow-velocity model for hydrokinetic energy availability assessment in the Amazon, *Acta Sci. Technol.* 42 (2020) e45703.
- [55] C.M. Niebuhr, M. Van Dijk, V.S. Neary, J.N. Bhagwan, A review of hydrokinetic turbines and enhancement techniques for canal installations: Technology, applicability and potential, *Renew. Sustain. Energy Rev.* 113 (2019) 109240.
- [56] R. Lacal-Arántegui, Globalization in the wind energy industry: contribution and economic impact of European companies, *Renew. Energy* 134 (2019) 612–628.
- [57] I. Kougiyas, T. Schleker, Hydropower technology development report 2018, 2019.
- [58] The world bank group, 2022, <https://wits.worldbank.org/CountryProfile/en/country/by-country/startyear/LTST/endyear/LTST/indicator/GC-TAX-IMPT-ZS>. Accessed: 2022-06-24.
- [59] M.T. Tigabu, D.D. Guta, B.T. Admasu, Economics of hydro-kinetic turbine for off-grid application: A case study of Gumara River, Upper Blue Nile, Amhara, Ethiopia, *Int. J. Renew. Energy Res. (IJRER)* 9 (3) (2019) 1368–1375.
- [60] N. Fontana, G. Marini, E. Creaco, Comparison of PAT installation layouts for energy recovery from water distribution networks, *J. Water Resour. Plan. Manag.* 147 (12) (2021) 04021083.
- [61] Global petrol prices, 2021, https://www.globalpetrolprices.com/Brazil/electricity_prices/. Accessed: 2021-11-09.
- [62] The world bank group, 2021, <https://data.worldbank.org/indicator/EG.USE.ELEC.KH.PC?locations=BR>. Accessed: 2021-11-09.
- [63] International monetary fund, 2021, <https://www.imf.org/en/Home>. Accessed: 2021-11-09.
- [64] P.P. Peterson, F.J. Fabozzi, *Capital Budgeting: Theory and Practice*, Vol. 10, John Wiley & Sons, 2002.
- [65] S. Subhra Mukherji, N. Kolekar, A. Banerjee, R. Mishra, Numerical investigation and evaluation of optimum hydrodynamic performance of a horizontal axis hydrokinetic turbine, *J. Renew. Sustain. Energy* 3 (6) (2011) 063105.
- [66] N. Kolekar, A. Vinod, A. Banerjee, On blockage effects for a tidal turbine in free surface proximity, *Energies* 12 (17) (2019) 3325.
- [67] P.K. Modali, A. Vinod, A. Banerjee, Towards a better understanding of yawed turbine wake for efficient wake steering in tidal arrays, *Renew. Energy* (2021).
- [68] J.D. Betancur, J.G.A. Marin, E.L.C. Arrieta, Design and hydrodynamic analysis of horizontal-axis hydrokinetic turbines with three different hydrofoils by CFD, *J. Appl. Eng. Sci.* 18 (4) (2020) 529–536.
- [69] A.K. Sleiti, Tidal power technology review with potential applications in gulf stream, *Renew. Sustain. Energy Rev.* 69 (2017) 435–441.
- [70] J. VanZwieten, W. McAnally, J. Ahmad, T. Davis, J. Martin, M. Bevelhimer, A. Cribbs, R. Lippert, T. Hudon, M. Trudeau, In-stream hydrokinetic power: Review and appraisal, *J. Energy Eng.* 141 (3) (2015) 04014024.
- [71] D. Micallef, T. Sant, A. Aissaoui, A. Tahour, A review of wind turbine yaw aerodynamics, in: *Wind Turbines-Design, Control and Applications*, IntechOpen, 2016.
- [72] I. Masters, J. Chapman, M. Willis, J. Orme, A robust blade element momentum theory model for tidal stream turbines including tip and hub loss corrections, *J. Mar. Eng. Technol.* 10 (1) (2011) 25–35.
- [73] M.M. Nunes, R.C. Mendes, T.F. Oliveira, A.C.B. Junior, An experimental study on the diffuser-enhanced propeller hydrokinetic turbines, *Renew. Energy* 133 (2019) 840–848.
- [74] C. Stadler, J. Wack, S. Riedelbauch, Investigation of the operating principle of diffuser augmented hydrokinetic turbines, in: *IOP Conference Series: Earth and Environmental Science*, Vol. 774, IOP Publishing, 2021, 012138.
- [75] P.A. Silva, D.A.R. Vaz, V. Britto, T.F. de Oliveira, J.R. Vaz, A.C.B. Junior, A new approach for the design of diffuser-augmented hydro turbines using the blade element momentum, *Energy Convers. Manage.* 165 (2018) 801–814.
- [76] T. Rezek, R. Camacho, N. Manzanares Filho, E. Limacher, Design of a hydrokinetic turbine diffuser based on optimization and computational fluid dynamics, *Appl. Ocean Res.* 107 (2021) 102484.
- [77] K. Loenbaek, C. Bak, J.I. Madsen, M. McWilliam, A method for preliminary rotor design-part 1: Radially independent actuator disk model, *Wind Energy Sci. Discuss.* 2020 (2020) 1–21.
- [78] V. Morcos, Aerodynamic performance analysis of horizontal axis wind turbines, *Renew. Energy* 4 (5) (1994) 505–518.
- [79] A. Suresh, S. Rajakumar, Design of small horizontal axis wind turbine for low wind speed rural applications, *Mater. Today Proc.* 23 (2020) 16–22.
- [80] C. Silva, D. Oliveira, L. Barreto, R. Bascopé, A novel three-phase rectifier with high power factor for wind energy conversion systems, in: *2009 Brazilian Power Electronics Conference, IEEE, 2009*, pp. 985–992.
- [81] M.L. Buhl Jr., New Empirical Relationship Between Thrust Coefficient and Induction Factor for the Turbulent Windmill State, Technical report, National Renewable Energy Lab.(NREL), Golden, CO (United States), 2005.